Ultraviolet Photometric Parameters of the Icy Galilean Satellites

Amanda R. Hendrix

Jet Propulsion Laboratory

California Institute of Technology

and

Deborah L. Domingue and Kimberly King**

Applied Physics Laboratory

Johns Hopkins University

** high school mentor student

Introduction.

Background.

The Galilean satellites are each phase-locked with Jupiter, so that one hemisphere (the Jovian hemisphere, centered on 0° longitude) is always facing Jupiter. The leading hemisphere is centered on 90° W longitude, while the central longitude of the trailing hemisphere is 270° W. Because Jupiter's magnetosphere corotates at a rate faster than the orbital speed of the moons, the satellites' trailing hemispheres are affected by magnetospheric particle bombardment. Some effects are implantation of magnetospheric ions, sputtering, erosion and grain size alteration. The leading hemispheres of these moons are more dominantly affected by micrometeorite bombardment, while the Jovian hemispheres may be affected by dust and/or neutral wind particles streaming out radially from Io and its torus.

Europa's surface displays a longitudinal albedo variation from leading to trailing hemisphere seen at visible wavelengths (Stebbins, 1927, Stebbins and Jacobsen, 1928, Millis and Thompson, 1975, Morrison *et al.*, 1974, Johnson *et al.*, 1983, McEwen, 19886, Nelson *et al.*, 1986.). The longitudinal albedo variation, or hemispherical albedo dichotomy, is a distinctive signature where the surface albedo varies as a cosine function and is lowest at the apex of the trailing hemisphere (270° W), and gradually increases to a maximum at the apex of the leading hemisphere (90° W) (Johnson *et al.*, 1983, McEwen,

1986, Nelson et al., 1986) and has been attributed to the preferential ion bombardment of the trailing side (Johnson et al., 1988, Popsieszalska and Johnson, 1989). The implanted ions originate in Io's torus and are picked up by Jupiter's magnetosphere. Lane et al. (1981) first noted, using IUE data, an absorption feature centered at 280 nm that appeared preferentially on Europa's trailing hemisphere. Subsequent observations with HST have also detected this trailing hemisphere absorption feature (Noll et al., 1995). Lane et al. (1981) proposed that this absorption was due to an S-O bond lattice, which produces an absorption feature resembling SO_2 gas. An alternative explanation for the 280 nm absorption feature is that the absorption band is due to SO_2 frost layered over water frost (Noll et al., 1995). The HST spectra of this feature agree well with the laboratory data of Sack et al. (1992) of layered SO_2/H_2O frost. This may imply an endogenic origin for the SO_2 with the magnetospheric bombardment creating erosion to expose the underlying SO_2 frost on the trailing hemisphere. Recent disk-resolved observations of Europa's trailing hemisphere by the Galileo UVS indicate that Europa's surface is darkest near 270° W and increases in brightness away from the trailing hemisphere apex. The 280 nm absorber, however, is much more confined to the trailing hemisphere apex region and may thus be caused by a slightly different process than the darkening. It was proposed that corotating ions are implanted into Europa's surface more deeply close to the trailing hemisphere apex, causing both the darkening and the 280 nm feature; away from 270° W,

the ions are implanted less deeply, causing some darkening but much lower amounts of the 280 nm feature (Hendrix et al., 1998a).

For wavelengths longer than 280 nm, Ganymede displays similar hemispherical albedo variations as Europa; however, at shorter wavelengths this hemispherical albedo dichotomy reverses itself (Stebbins, 1927, Stebbins and Jacobsen, 1928, Millis and Thompson, 1975, Morrison et al., 1974, Nelson et al., 1987). The longitudinal albedo variations on both Europa and Ganymede is correlated to the preferential bombardment of the trailing hemisphere by magnetospheric ions (Lane et al., 1981, Nelson et al., 1987, Johnson, 1988, Pospieszalska and Johnson, 1988). However, on Ganymede a different absorber or the presence of an additional absorber is needed to explain the hemispherical dichotomy; Nelson et al. (1987) have proposed that the feature is ozone in addition to sulfur. More recent HST observations by Noll et al. (1996) have confirmed Nelson et al.'s (1987) preliminary evidence for the presence of ozone on Ganymede's trailing hemisphere with the detection of an absorption band centered at 260 nm. Recent disk-resolved observations by the Galileo UVS indicate an increase in a 260 nm absorption feature near Ganymede's north and south poles (Hord et al., 1996). In addition to the exogenic alterations due to ion implantation, sublimation (at low latitudes) and redeposition (at mid- to high latitudes) also play a role in surface alterations (such as grain size changes) that should be detectable through photometric modeling. Ganymede is less subject to surface alterations due to magenetospheric bombardment than Europa,

due to lower ion fluxes at 15 RJ; however, Ganymede's lower albedo, and thus higher surface temperature, mean that sublimation is more important at Ganymede than at Europa. An alternative explanation for Ganymede's 260 nm feature is that an "ozone-like" absorber is concentrated in regions of high water ice amounts (such as the polar caps). Alternately, the absorber in the polar regions may be caused by additional bombardment there by particles traveling along Ganymede's magnetic field lines.

Callisto displays the opposite hemispherical dichotomy as the other two icy galilean satellites, as its trailing hemisphere has a slightly higher albedo than its leading hemisphere. This characteristic is ascribed to preferential micrometeorite bombardment of the leading hemisphere. Magnetospheric ion bombardment (and its associated sputtering, implantation and grain size alteration) is a weaker alteration process at Callisto's orbit compare to at Europa and Ganymede. An interesting absorption feature has been detected on Callisto (Lane and Domingue, 1997, Noll *et al.*, 1997) which greatly resembles the 280 nm absorption feature seen on Europa. This feature on Callisto has been detected on the leading Jovian-facing hemisphere, in constrast to Europa, where it is seen on the trailing hemisphere. The correlation with the Jovian-facing hemisphere suggests a possible formation by neutral sulfur implantation from the Jovian neutral wind (Lane and Domingue, 1997). Galileo UVS observations of Callisto (Hendrix *et al.*, 1998b, 1997a) confirm that Callisto's weak 280 nm band is concentrated on the Jovian

leading hemisphere and is associated with dark material rather than the central basin of the Valhalla impact feature.

Goals of this work

In this study, disk-integrated observations of the icy galilean satellites from the International Ultraviolet Explorer (IUE), the Hubble Space Telescope (HST) and the Galileo Ultraviolet Spectrometer (UVS) were used to determine the Hapke photometric parameters of the satellites for different longitudes at several ultraviolet wavelengths. Our objectives are to determine the Hapke parameters of the icy galilean satellites at ultraviolet wavelengths, to look for longitudinal variations, wavelength variations. Such a study will help us further understand the icy galilean satellites, and will also serve to further our understanding of the usefulness of the Hapke model, since it has previously only been used at visible wavelengths. The values of many of the Hapke model parameters are expected to vary with wavelength. These variations can be used to define the optical and scattering natures of the materials comprising the surface regolith. Our goal is the understand how the environment of the jovian system alters the optical and mechanical properties of the regoliths of the icy satellites.

The optical and mechanical properties of the surfaces of the icy galilean satellites from photometric modeling using Hapke's theory are well studied in the visible wavelength region (Buratti, 1985, 1991; Domingue *et al.* 1991, 1995; Domingue and

Hapke, 1992; Domingue and Verbiscer, 1997; Helfenstein, 1986). Similar modeling of data from far- to near-ultraviolet observations has not yet been accomplished because complete modeling requires data at a wide range of phase angles. The Galileo UVS data are the first-ever disk-resolved and high-phase angle observations of the galilean satellites at these wavelengths. Used in combination with the low phase angle IUE and HST data, the UVS data provide an excellent opportunity to use Hapke's photometric funtion to model the photometric parameters of the icy galilean satellites for the first time at ultraviolet wavelengths. Furthermore, we investigate additional endogenic and exogenic processes affecting the surfaces of the satellites by exploring not just the leading and the trailing hemispheres, but also the jovian and anti-jovian regions.

Data Sets and Data Reduction.

In order to utilize the Hapke model in a meaningful way, a data set with a wide phase angle range must be used. It is to this end that we combined the IUE and HST observations (mostly smaller phase angles, <12°) with the Galileo UVS data (mostly larger phase angles, but also some comparable to IUE and HST). The data sets, including observations from IUE, HST and Galileo, are listed in Tables I, II and III for Europa, Ganymede and Callisto, respectively. The tables list the observation name, the solar phase angle and the sub-Earth (or sub-spacecraft, in the case of the Galileo observations) longitude

The IUE data used in this study were obtained from the INES (IUE Newly-Extracted Spectra) website. The NEWSIPS versions of these spectra have been published elsewhere (Nelson et al.; Lane and Domingue). The INES files benefit from an improved geometric correction, a more accurate photometric correction and an increased signal-to-noise ratio of the extracted IUE data through the use of new processing algorithms (Wamsteker and Gonzelez-Riestra, 1998). The IUE observations of the icy galilean satellites span the 1978-1996 time period. Spectra were taken with the Long Wavelength Prime and Redundant (LWP and LWR) spectrographs that covers the 185-335 nm wavelength range with a spectral spacing of 0.27 nm.

The HST data were obtained from the MAST archive and are spectra that have previously been published elsewhere (Noll, et al.). The Faint Object Spectrograph (FOS) observations cover the 222-330 nm wavelength range with a spectral spacing of 0.05 nm.

To determine the reflectance measured in the IUE and HST observations, we subtracted off the small amount of background measurement (first several spectral elements averaged), then converted the spectra to photons/cm^2-sec-Å for division by the solar spectrum. For all observations, we used a solar spectrum from UARS SOLSTICE (Rottman), corrected to a Earth-Sun distance of 1.0 AU. The observations were corrected for satellite-Sun and satellite-Earth distances at the time of each measurement.

The Galileo observations used in this study were taken using the UVS F-channel (162-323 nm, with a 0.32 nm spectral element spacing). Some of the spectra were

previously published (Hendrix et al. Europa DPS Tucson poster, Europa paper – phase curve, Ganymede paper – phase curve.) For each observation, the background signal was subtracted, then the calibration curve applied; generally the background signal is due to radiation background and is approximated by averaging the first ~100 spectral elements, or the signal shortward of ~ 200 nm, where no reflected sunlight is measured. In determining the reflectance the filling factor was accounted for, since these disk-integrated observations were performed at distances such that the 0.1°x0.4° F-channel FOV was not filled.

In this analysis, the data were binned into 7 wavelength groups to study any spectral variations in Hapke parameters. The reflectance in each wavelength bin was determined by averaging over 21 spectral samples for IUE and Galileo data, and 114 samples for HST data. The seven wavelength bins are 260, 270, 280, 290, 300, 310 and 320 nm, each with a 6 nm bandpass.

Analysis.

Rotational Phase Curves.

Disk-integrated brightness variations in planetary observations are governed by variations due to rotational phase (which part of the planet you are observing) and to solar phase (the viewing geometry of the observation). In order to study and model solar phase brightness variations the changes in brightness due to rotational phase must first be

accounted for. For each of the icy Galilean satellites we studied, we used the IUE data set

to establish the UV rotational phase curves. The rationale in using only the IUE data is

that it removes variations due to different instrumentation and the IUE data set spans such

a short range of solar phase values that we can assume the solar phase brightness

contribution is constant within this data set.

The IUE data set spans 2.9 to 11.4 degrees in solar phase angle for each of the

satellites. Nelson *et al.* (1987) used this span of solar phase angles to first measure the

UV rotational phase curves of all four Galilean satellites using IUE observations. The

rotational phase curve analysis presented here also uses the entire span of solar phase

data, and also includes IUE data taken since the Nelson *et al.* (1987) work. The data set

for each satellite was put into wavelength bins. Each wavelength data set for each

satellite was analyzed in the same manner.

A rotational phase curve of the form $R = m\theta + b + A[\cos((2\pi\theta/P) + \rho)]$ was

initially fit to each data set (as a function of satellite and wavelength), where R is the

calculated brightness (or reflectance), θ is the rotational phase angle, and the parameters

m, b, A, P, and ρ (hereafter referred to as the rotational variables) are constants. The

rotational variables were found by minimizing the root mean square (RMS) values

between the measured IUE reflectance and the calculated brightness. Once a solution to

the rotational phase curve was found for all wavelengths, the goodness of fit between the

300 nm observations and the calculated rotational phase curve was examined. All data within the 300 nm data set that varied by more than 15% of the predicted value from the fitted rotational phase curve were tagged as suspicious. The spectral data corresponding to these data points were removed from the IUE data set and not used in our analysis. The rotational phase curve equation was then refit to the remaining data using the same algorithm. Once again those 300 nm observations that varied by more than 15% of the new solution were removed from the spectral data set and the rotational phase curve equation was refit to the remaining data. This solution to the rotational phase curve equation was then used to define the rotational phase curve behavior for that particular data set. The remaining IUE data points plus the HST and Galileo observations (hereafter referred to as the refined data set) were then used for the solar phase curve analysis.

Solar Phase Curves.

Rotational phase corrections for the refined data set were made based on the solutions to the rotational phase curve equation described above. For each satellite the refined data set was divided into four groups as a function of longitude: 1) leading hemisphere data, 2) trailing hemisphere data, 3) Jovian hemisphere data, and 4) anti-Jovian hemisphere data. The leading hemisphere data group contains those observations taken between 0 and 180° longitude and was corrected to 90° rotational phase. The trailing hemisphere data group contains those observations taken between 180 and 360°

longitude and was corrected to 270° rotational phase. The Jovian hemisphere data group contains those observations taken between 0 and 90° longitude and 270 and 360° longitude. This group of data was corrected to 0° rotational phase. The anti-Jovian hemisphere data group contains those observations taken between 90 and 270° longitude and was corrected to 180° rotational phase.

The IUE data fall within four solar phase curve ranges: 1) $2.8° \pm 0.2°$, 2) $6.5° \pm 0.2°$, 3) $10.5° \pm 0.8°$, and 4) $8.3° \pm 1°$. The data in these ranges were corrected for rotational phase variations and then averaged. The resulting average angles and brightnesses were used in the solar phase curve data sets along with the HST and Galileo observations.

Hapke Analysis.

The resulting solar phase curves, for each wavelength bin, were modeled using Hapke's model (Hapke, 1984, 1986). Hapke's model was chosen since the visible solar phase curves for the icy Galilean satellites have been examined with this same model (Domingue and Verbiscer, 1997), and comparisons with the visible modeling results can be easily discussed. The model was fit to each wavelength data set using a root mean square grid search. This same algorithm and software was used to fit the Hapke model to the visible solar phase curve observations of these satellites (Domingue and Verbiscer, 1997).

The Hapke model parameters include ω (single scattering albedo), B_0 (shadow-hiding opposition amplitude), h (shadow-hiding opposition half-width), θ-bar (surface roughness), and the single particle scattering function parameters b & c. The single particle scattering function, $P(\alpha)$, used in this analysis is the double Henyey-Greenstein function of the form

$$P(\alpha) = \frac{(1-c)(1-b^2)}{\left[1-2b\cos\alpha + b^2\right]^{3/2}} + \frac{c(1-b^2)}{\left[1+2b\cos\alpha + b^2\right]^{3/2}} .$$

The mathematical details of the Hapke model used can be found in Hapke (1984) and Hapke (1986). This form of the model assumes that the opposition surge is created by the shadow-hiding process and does not account for the coherent-backscatter process. This will affect the interpretation of the results. However, this modeling effort is similar to that published for the visible solar phase curves and will allow for interpretations based on comparisons with past modeling efforts of the icy Galilean satellites and other objects within the solar system (such as the Moon).

Results.

Rotational Phase Curves

Figure X1 shows the rotational phase curve fit to the 300 nm observations for each of the satellites. This figure demonstrates that the rotational equation used to model the data provides a good measure (less than 2% RMS variability) of the reflectance trends with rotational phase. The RMS values for the 300 nm fit are 0.012, 0.006, and 0.003 for Europa, Ganymede, and Callisto, respectively, with the respective range of RMS values over all the wavelengths being 0.01-0.017, 0.005-0.009, and 0.003-0.004.

The calculated rotational phase curves as a function of wavelength for each satellite are shown in Figure X2. The rotational phase curves become systematically brighter as wavelength increases from 260nm to 310nm for all the satellites. The rotational phase curves are similar at 310nm and 320nm for each satellite. For Europa the leading hemisphere increases in brightness with increasing wavelength more rapidly than the trailing hemisphere. This makes the amplitude in the cosine behavior of the rotational phase curve larger as wavelength increases. No similar hemispherical trends are seen in the Ganymede or Callisto rotational phase curves.

Hapke Fits

Table Z1 lists the Hapke model parameter values for Europa. Similar modeling results for Ganymede and Callisto are provided in Tables Z2 and Z3, respectively. Table

Z4 lists the comparable visible wavelength Hapke parameter values (Domingue and

Verbiscer, 1997) for each of the satellites.

Discussion.

VARIATION IN HAPKE PARAMETERS WITH LONGITUDE

Europa

There is some scatter in the solar phase curves of Europa, particularly in the

leading and jovian hemisphere data sets, but at this point we can say the following.

Depends on the wavelength and the case (holding parameters constant).

Single-scatter albedo. This parameter varies like the orbital phase curve (i.e.,

reflectance is dominated by single scatter albedo). LH brightest, TH darkest, Jov and AJ

are in-between. Trend is generally the same at all wavelengths, although at a couple of

wavelengths, the anti-jovian w is not much lower than the leading w (may not be

significant). At 320 nm, the orbital w curve of Europa is much shallower than at the

shorter wavelengths – the TH w is not a whole lot lower than the LH w, compared to

other wavelengths.

Phase function terms. We see a distinct longitudinal variation in both b and c,

where b and c are both greater on the anti-jovian and trailing hemispheres than on the

leading and jovian hemispheres. The most obvious comparison is between the jovian and

anti-Jovian hemispheres: the jovian hemisphere is more backscattering than the anti-jovian, and may have less of a forward scattering component. The leading and trailing hemisphere have similar scattering functions, and we probably can't draw any conclusions about differences due to scatter in the data sets.

Opposition effect terms. At 260 nm we determine B0 values other than 0, but this is the only wavelength, except on the anti-Jovian hemisphere. This may indicate that this data set is not appropriate for measuring Europa's opposition effect. In case 1, the h value was set – so we see no variation with longitude, by definition. In cases 2 and 3, it was allowed to vary. In these cases, we still see no significant variation with longitude. In most cases, the h value ended up being ~0.09

Roughness. The fact that we get quite a bit of scatter in best-fit theta-bar values when we don't hold this parameter constant indicates that we do not have a good data set do determine this parameter, and that the variations that we come up with are not meaningful. Thus, we do not see meaningful variation in theta-bar with wavelength or longitude, and it is best to hold this parameter constant since we do not have the data set to constrain it.

Conclusions.

Table I. Europa Disk-Integrated Observations

Instrument/observation	Phase angle	Central longitude
HST	5.2	TH
HST	4.3	LH
LWP02955	10.5	288
LWP02957	10.5	307
LWP02969	10.6	148
LWP06578	0.1	242
LWP29988	10.2	252
LWP29991	10.2	275
LWP29995	10.2	287
LWP29998	10.2	297
LWP30014	10.3	117
LWP30015	10.3	121
LWP30018	10.3	132
LWP30019	10.3	135
LWP30030	10.4	211
LWP30031	10.4	213
LWP30036	10.4	235
LWP30038	10.4	243
LWP30058	10.4	62
LWP30062	10.4	76
LWP30063	10.4	79
LWP30064	10.4	82
LWP32172	10.7	38
LWP32173	10.7	42
LWP32176	10.7	61
LWP32177	10.7	65
LWP32180	10.7	81
LWP32181	10.7	84
LWP32183	10.6	130
LWP32190	10.6	165
LWP32204	10.6	272
LWP32205	10.6	276
LWP32220	10.5	34
LWP32226	10.5	112
LWP32228	10.5	121

LWP32229	10.5	124
LWP32232	10.4	136
LWP32238	10.4	218
LWP32255	10.3	317
LWP32263	10.2	59
LWP32270	10.2	143
LWP32272	10.2	150
LWP32274	10.2	162
LWP32279	10.1	250
LWP32284	10.1	270
G8PH07	7.16	20
C3PH68	68.741	25
G8PH65	64.8	30
C9PH03	1.53	40
C9PH05	4.293	40
G1ECL01	48.983	40
G1ECL04	44.4735	50
G2PH60	60.76	45
C3PH57	57.25	50
C3PH57	56.84	50
G7ECL04	63.35	70
G7ECL01	68.08	60
C3PH40	39.3725	90
G2PH43	42.185	120
C3PH41	41	200
G2PH58	58	225
G2PH79	79	330
C10LON250	103.313	270
C10LON270	96.3847	280
C10LON290	81.8105	290
C10PH93	93.6	100
C10PH95	95.5	160
C10LON100	91.8	125
C10LON300	64.1	300

Table II. Ganymede Disk-Integrated Observations

Instrument/observation	phase angle	Central longitude
LWP29978	10.2	16
LWP29979	10.2	17
LWP29982	10.2	23
LWP29983	10.2	24
LWP29984	10.2	25
LWP29986	10.2	47
LWP04269	11.1	54
LWP05270	11.1	56
LWP29992	10.2	64
LWP29993	10.2	66
LWP29994	10.2	67
LWP04278	11.1	73
LWP04279	11.1	75
LWP29999	10.2	75
LWP03679	0.1	79
LWP09793	10.8	97
LWP02958	10.5	102
LWP02959	10.5	103
LWP30013	10.3	161
LWP30016	10.4	166
LWP06725	7.5	188
LWP09713	11.3	212
LWP30032	10.4	213
LWP30033	10.4	214
LWP05796	11.1	229
LWP05797	11.1	230
LWP06331	6.4	231
LWP06332	6.4	233
LWP30043	10.4	263
LWP30044	10.4	265
LWP30045	10.4	266
LWP05806	11.1	280
LWP02979	10.7	292
LWP05815	11.2	330
LWP05817	11.2	337

LWP30034	10.4	216
LWP30061	10.4	319
LWP30081	10.5	50
LWP30082	10.5	52
LWP30086	10.5	59
LWP30087	10.5	60
LWP30094	10.5	92
LWP30095	10.5	93
LWP30098	10.5	98
LWP30099	10.5	100
LWP30100	10.5	101
LWP32171	10.7	125
LWP32178	10.7	146
LWP32179	10.7	147
LWP32182	10.7	152
LWP32197	10.6	227
LWP32198	10.6	229
LWP32201	10.6	236
LWP32202	10.6	238
LWP32203	10.6	240
LWP32209	10.5	272
LWP32210	10.5	273
LWP32211	10.5	275
LWP32216	10.5	291
LWP32217	10.5	295
LWP32218	10.5	300
LWP32219	10.5	302
LWP32240	10.4	39
LWP32241	10.4	40
LWP32243	10.4	44
LWP32249	10.3	72
LWP32250	10.3	74
LWP32251	10.3	77
LWP32253	10.3	81
LWP32254	10.3	83
LWP32281	10.1	234
LWP32283	10.1	238
LWP32285	10.2	242
C3PH80	78.46	300

E4PH87	86.71	315
G8PH68	67.63	120
E11 PH00	1.27	340
C10PH77	77.16	30
HST	4.8	71
HST	6.7	255

Table III. Callisto Disk-Integrated Observations

Instrument/observation	Phase angle	Central longitude
HST	9.3	91.8
HST	10.1	279.4
LWP30028	10.4	19
LWP30029	10.4	20
LWP30035	10.4	25
LWP30046	10.4	45
LWP30047	10.4	46
LWP30048	10.4	47
LWP30059	10.4	66
LWP30060	10.4	67
LWP30065	10.4	71
LWP04274	11.1	74
LWP30078	10.5	106
LWP30079	10.5	107
LWP30083	10.5	111
LWP30084	10.5	112
LWP30085	10.5	112
LWP30096	10.5	130
LWP30097	10.5	131
LWP30101	10.5	134
LWP30102	10.5	134
LWP30103	10.5	135
LWP06727	7.7	136
LWP09792	10.8	157
LWP09714	11.3	259
LWP02971	10.6	286
LWP29976	10.2	297
LWP29977	10.2	297
LWP29980	10.2	299
LWP29981	10.2	300
LWP29985	10.2	311
LWP29990	10.2	317
LWP29996	10.2	321
LWP29997	10.2	322
LWP32184	10.6	246

LWP32185	10.6	247
LWP32187	10.6	250
LWP32188	10.6	251
LWP32189	10.6	252
LWP32192	10.6	258
LWP32193	10.6	259
LWP32195	10.6	267
LWP32196	10.6	268
LWP32199	10.6	270
LWP32200	10.6	271
LWP32206	10.6	278
LWP32207	10.6	279
LWP32208	10.6	279
LWP32212	10.5	291
LWP32213	10.5	291
LWP32215	10.5	293
LWP32227	10.5	319
LWP32230	10.5	321
LWP32237	10.4	340
LWP32265	10.2	25
LWP32266	10.2	26
LWP32267	10.2	27
LWP32268	10.2	27
LWP32271	10.2	42
LWP32273	10.2	43
LWP32275	10.2	46
LWP32276	10.2	47
LWP32277	10.2	48
LWP32278	10.1	63
LWP32282	10.1	66
G8PH78	77.78	140
E11PH89	90.053	90
E11PH61	61.612	90

Figure Captions

Final orbital phase curves for each satellite at each wavelength

Solar phase curves for each satellite hemisphere at each wavelength

Hapke parameters vs. longitude for each satellite at each wavelength

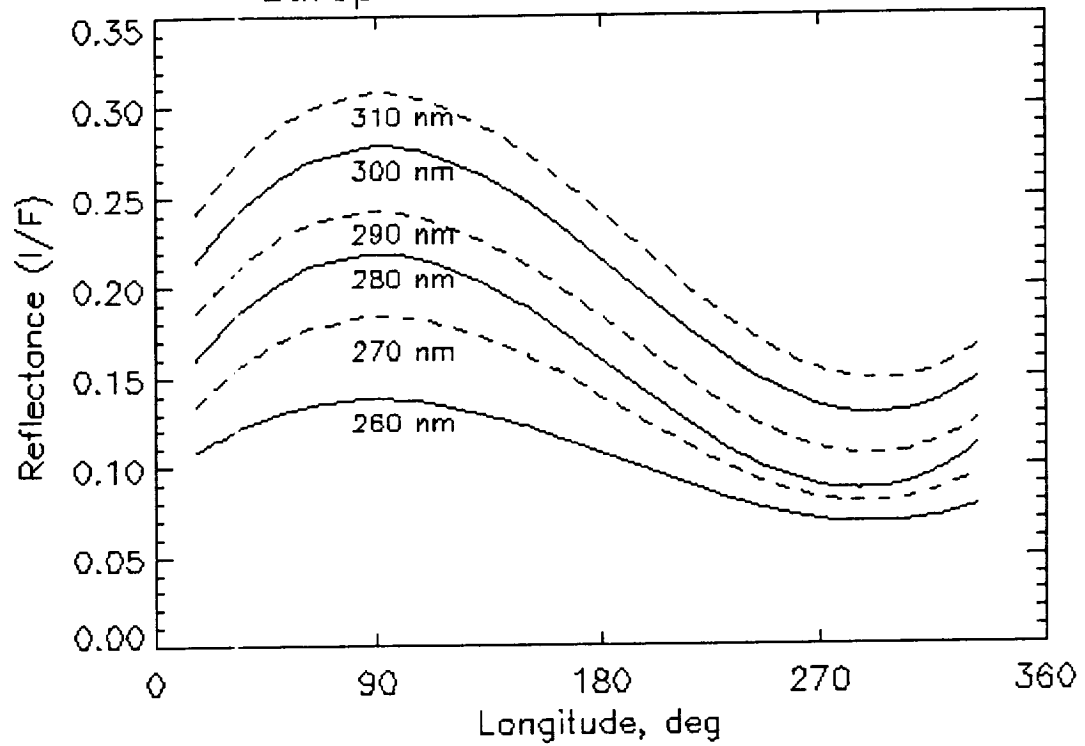Hapke parameters vs. wavelength for each satellite hemisphere

Figure Y1. Comparisons of the rotational phase curves derived for each of the icy Galilean satellites at 300nm. The comparison is between initial rotational phase curve (line with + signs) fits using the total data set versus the final rotational phase curves (line with no symbol) derived from the refined data set. The differences between these two curves seen at 300nm are representative of the differences observed at the other UV wavelengths examined.

Figure X1. Rotational lightcurves of the icy Galilean satellites at 300nm. The observations (diamonds) are from the refined IUE data set. The solid line represents the best fit rotational phase curve. The RMS values between the curves and the data are 1.2%, 6%, and 3% for Europa, Ganymede, and Callisto, respectively.
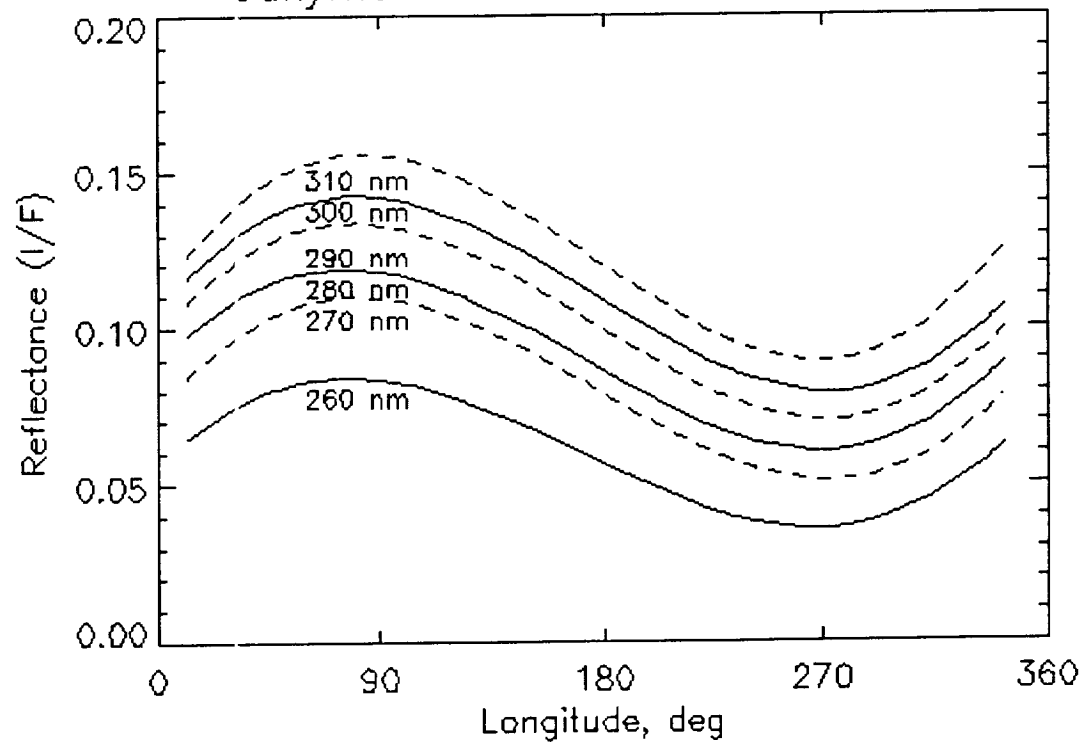
Figure X2. The final rotational phase curves for each of the icy Galilean satellites as a function of wavelength.
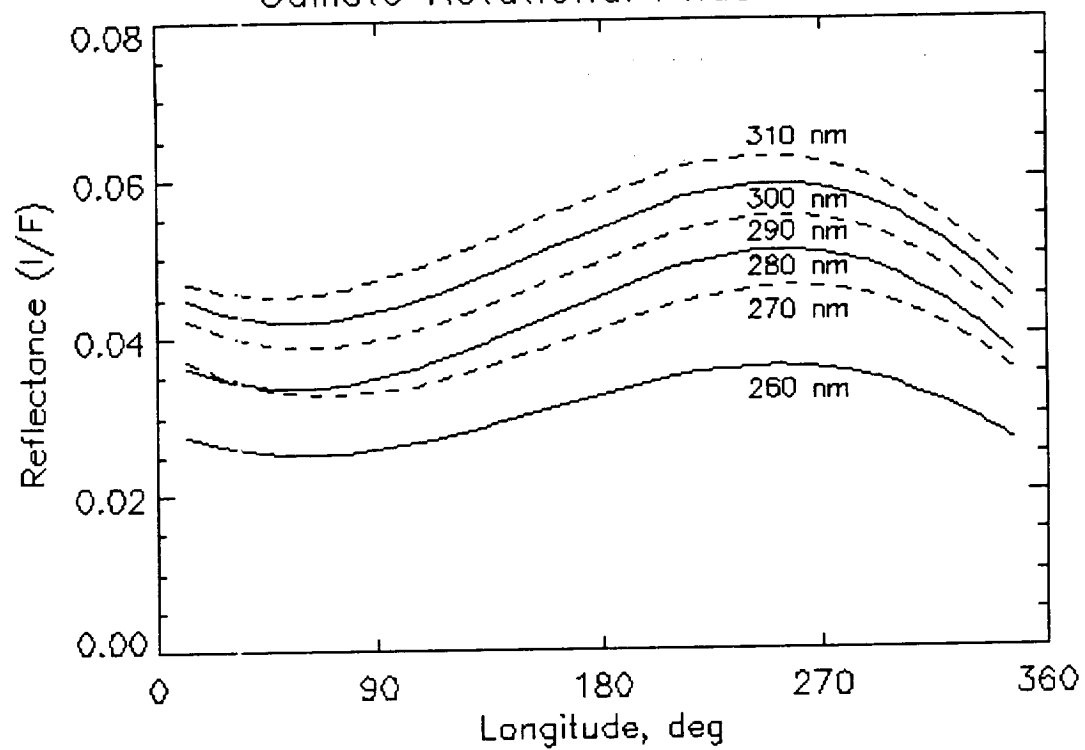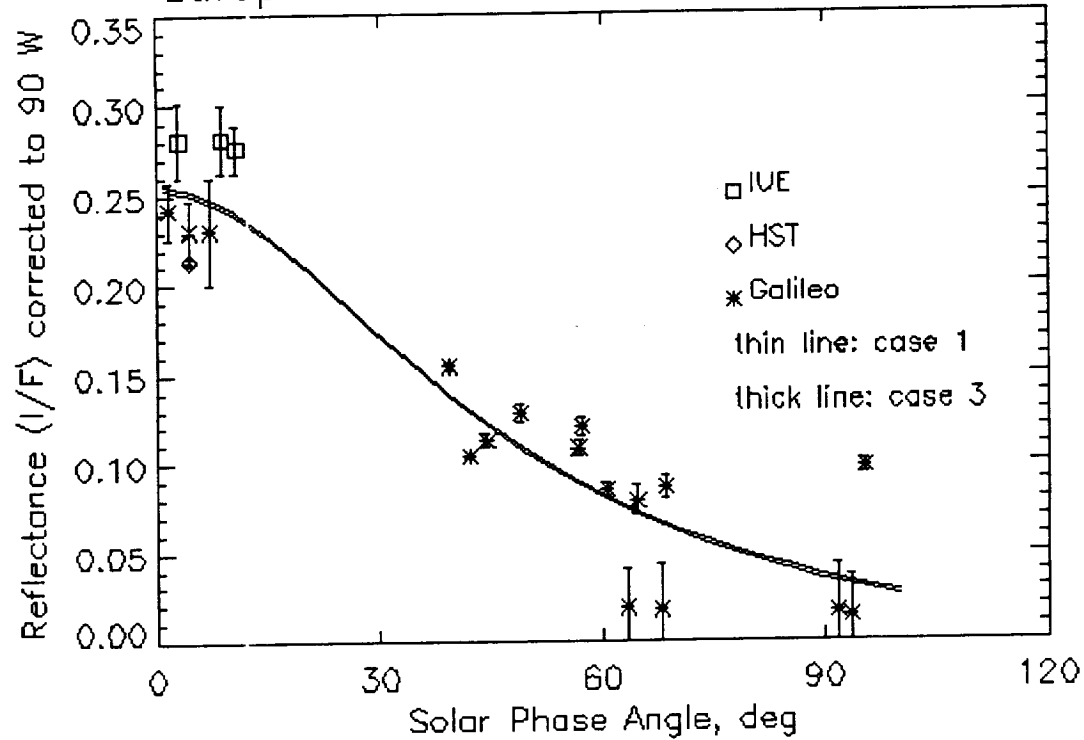
Europa
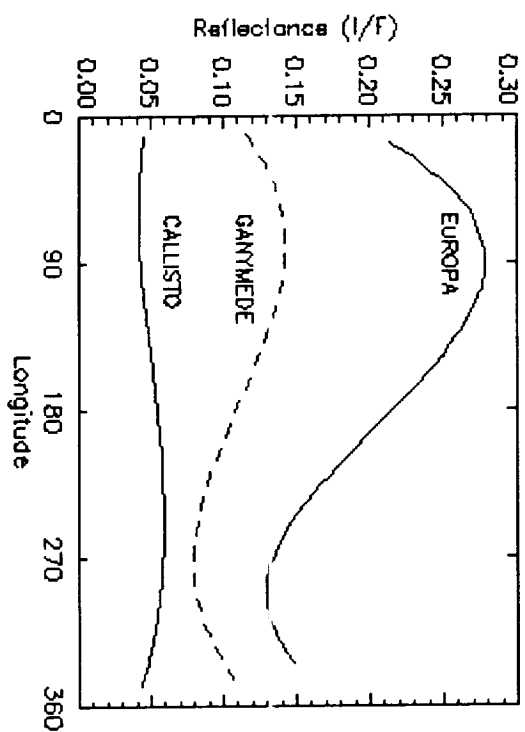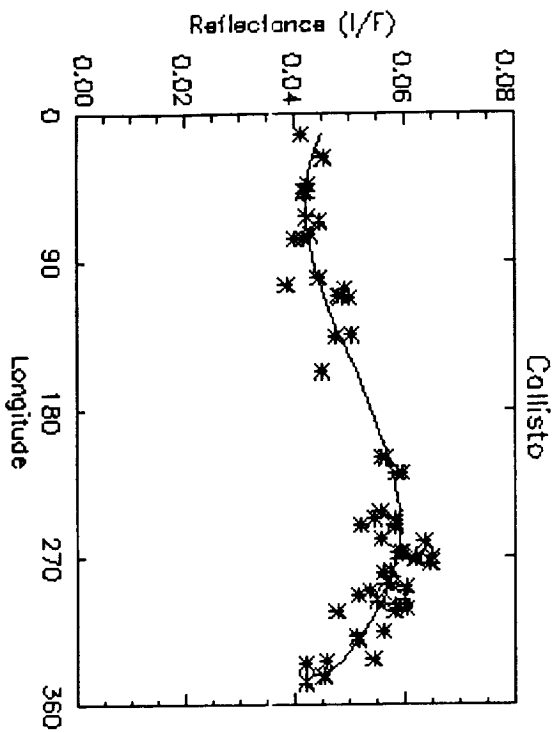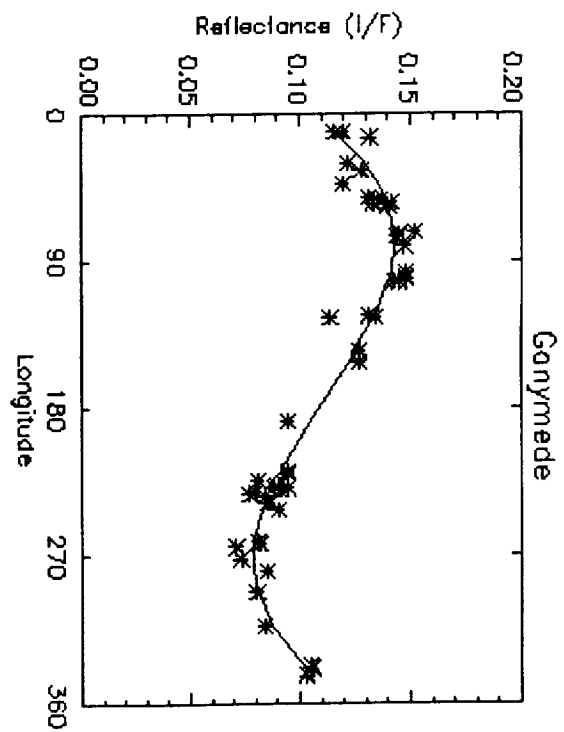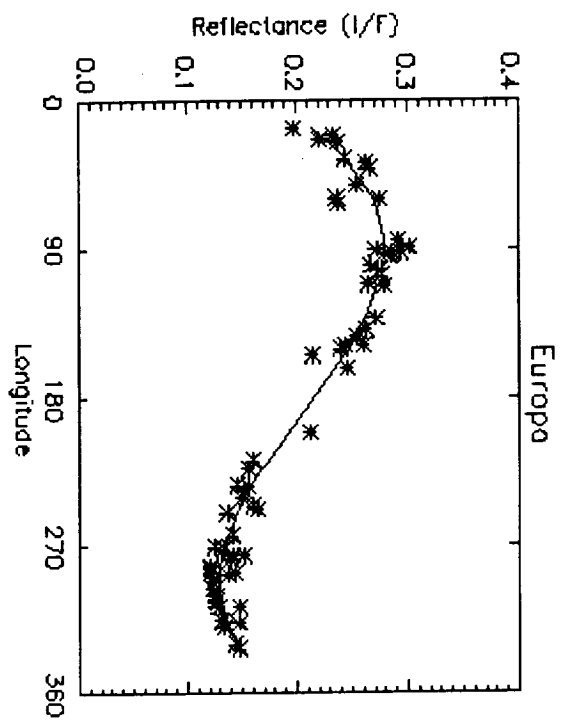
Ganymede

Callisto

Europa Rotational Phase Curves

Ganymede Rotational Phase Curves

Callisto Rotational Phase Curves

Figure showing Reflectance (I/F) versus Longitude, deg for Callisto. Curves labeled 310 nm, 300 nm, 290 nm, 280 nm, 270 nm, and 260 nm.

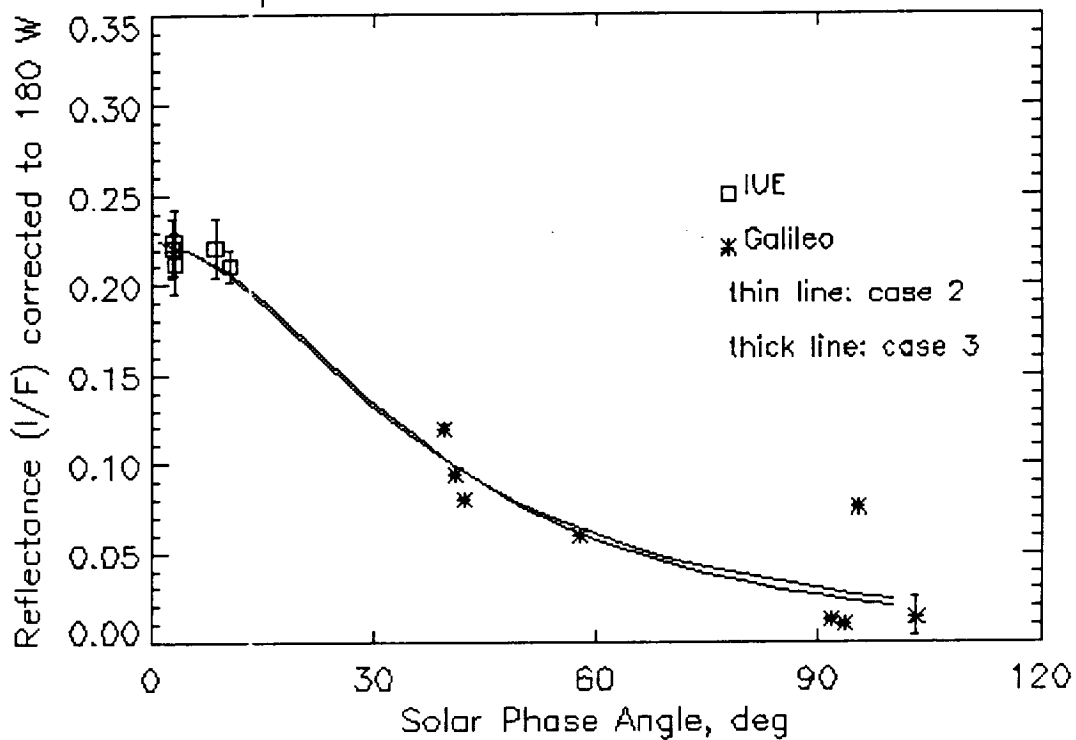Europa LH Solar Phase Curve at 300 nm

Europa AJ Solar Phase Curve at 300 nm

Europa TH Solar Phase Curve at 300 nm

Europa Jov Solar Phase Curve at 300 nm